Article

Cervical Cancer Tissue Analysis Using Photothermal Midinfrared Spectroscopic Imaging

Published as part of Chemical & Biomedical Imaging virtual special issue "Sub-diffraction Chemical Imaging".

Reza Reihanisaransari, Chalapathi Charan Gajjela, Xinyu Wu, Ragib Ishrak, Yanping Zhong, David Mayerich, Sebastian Berisha, and Rohith Reddy*

Read Online

ACCESS | Metrics & More | Article Recommendations

ABSTRACT: Hyperspectral photothermal mid-infrared spectroscopic imaging (HP-MIRSI) is an emerging technology with promising applications in cervical cancer diagnosis and quantitative, label-free histopathology. This study pioneers the application of HP-MIRSI to the evaluation of clinical cervical cancer tissues, achieving excellent tissue type segmentation accuracy of over 95%. This achievement stems from an integrated approach of optimized data acquisition, computational data reconstruction, and the application of machine learning algorithms. The results are statistically robust, drawing from tissue samples of 98 cervical cancer patients and incorporating over 40 million data points. Traditional cervical cancer diagnosis methods entail biopsy, staining, and visual evaluation by a pathologist. This process is qualitative, subject to variations in staining and subjective interpretations, and requires extensive tissue processing, making it costly and time-consuming. In contrast, our proposed alternative can produce images comparable to those from histological analyses without the need for staining or complex sample preparation. This label-free, quantitative method utilizes biochemical data from HP-MIRSI and employs machine-learning algorithms for the rapid and precise segmentation of cervical tissue subtypes. This approach can potentially transform histopathological analysis by offering a more accurate and label-free alternative to conventional diagnostic processes.

KEYWORDS: O-PTIR, cervical cancer, photothermal, mid-infrared spectroscopic imaging, chemical imaging, label-free imaging
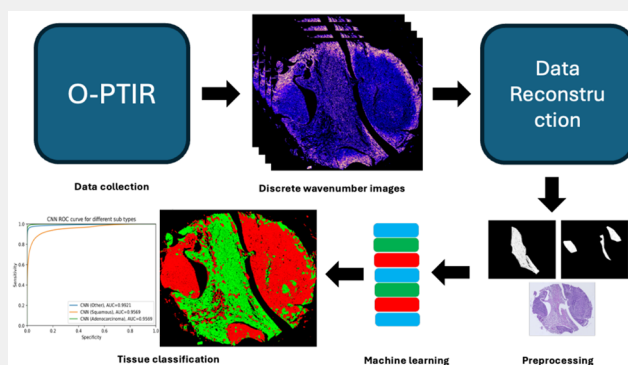
1. INTRODUCTION

Cervical cancer is a significant global health challenge, with over 600 000 new cases and 350 000 deaths per year.[1] Its primary cause is persistent infection with high-risk human papillomavirus (HPV) strains, alongside factors such as smoking, immunosuppression, long-term oral contraceptive use, and high parity.[2,3] As the fourth most common cancer in women, its impact varies widely by location with less developed areas suffering more due to limited healthcare, screening, and vaccination.[4] Despite prevention efforts, including HPV vaccination and screening in high-income communities, cervical cancer remains a major cause of death in lower-income communities across the world.[5] Early detection is key to improving survival outcomes, but many lack access to early screening, leading to late-stage diagnoses.[6]

Recent decades have seen major advancements in the early detection and diagnosis of cervical cancer. The Pap smear test, crucial for identifying precancerous or cancerous cells, has significantly contributed to lowering cervical cancer mortality rates.[7] Despite its utility, its accuracy is hindered by subjective sample interpretation, leading to overlooked lesions and false negatives. This limitation underscores the need for more objective and sensitive methods.

HPV DNA testing has become a preferred screening tool, detecting virus-induced cell changes with greater sensitivity than Pap smears and allowing less frequent testing.[8] Despite its effectiveness in identifying high-risk HPV strains, it risks overtreatment, particularly in younger women who might clear the virus naturally. Furthermore, it cannot verify the presence or stage of cancer, requiring additional diagnostics upon HPV detection.[9] Liquid biopsy, a noninvasive method for detecting
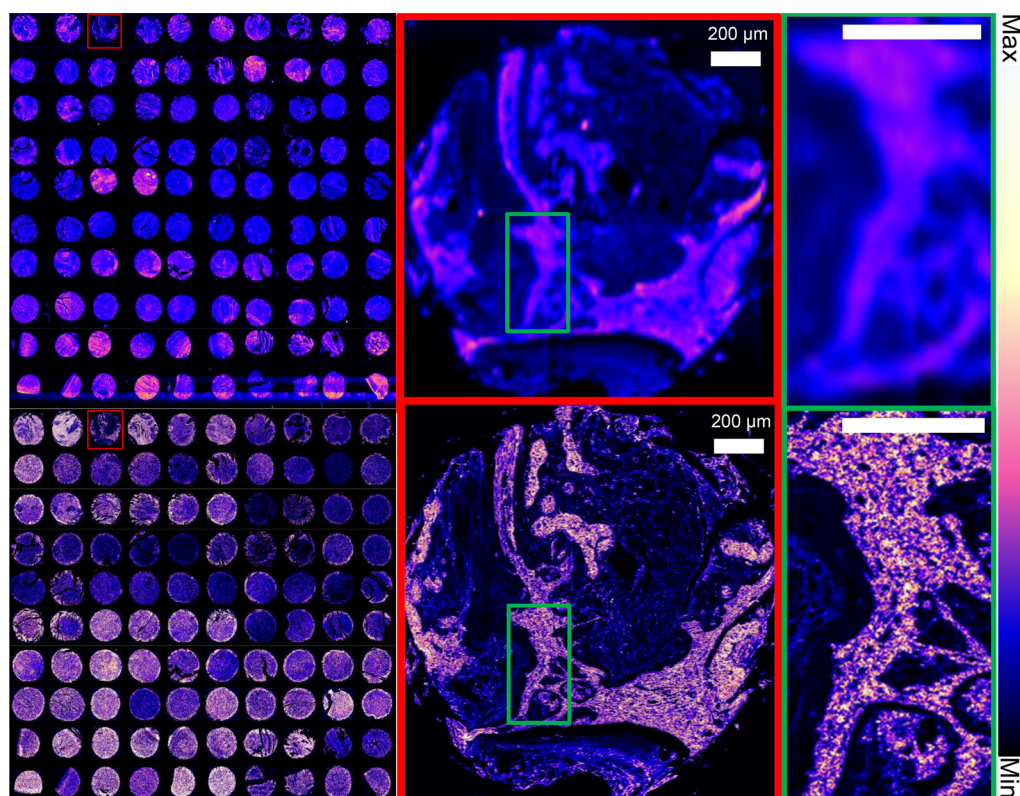
Figure 1. Experimental data from 100 cervical cancer patient cores measured using FTIR (top row) versus O-PTIR (bottom row) imaging at the amide I band (1660 cm^{-1}) at their highest resolutions. A zoomed-in comparison of the FTIR and O-PTIR data from the same core highlights the difference in resolution and image quality. O-PTIR surpasses the diffraction-limit barrier associated with FTIR systems, enabling imaging at 0.5 μm resolution.

cancer DNA in blood, holds promise for early cervical cancer detection, potentially improving treatment outcomes.[10] Yet, its performance varies due to technical factors and analysis of different HPV subtypes, highlighting its diagnostic and monitoring challenges.[11] Raman spectroscopy, proposed for diagnosing cervical cancer, offers biochemical specificity but encounters challenges due to long data acquisition times for hyperspectral imaging. The generation of accurate histological maps is difficult, with the results influenced by instrument settings and sample preparation.[12] Fluorescence lifetime imaging microscopy (FLIM) emerges as a rapid technique but lacks the biochemical specificity of infrared spectroscopy methods and faces segmentation accuracy issues, alongside reproducibility and accuracy concerns from variability in settings and preparation.[13,14] Diffuse reflectance (DR) spectroscopy, suggested for lesion discrimination, falls short in spatial resolution for histology and sensitivity for low-grade lesion differentiation.[15]

Improving cervical cancer histopathology using machine learning and artificial intelligence (AI) techniques has been proposed.[16,17] These algorithms are trained on large data sets of stained cervical cancer images, offering the potential for more precise and consistent detection of precancerous changes than human interpretation alone.[18] The training involves brightfield microscope images stained and annotated by pathologists, serving as the ground truth, promising to improve screening program efficiency and effectiveness.[19] However, the "black box" nature of machine learning models, especially deep learning, presents challenges, such as the absence of clear, biochemically specific explanations for results, which may lead

to reluctance among doctors to adopt these technologies in clinical settings. Moreover, these models require vast amounts of high-quality, well-labeled data for effective training and generalization, a significant hurdle given the variability in staining techniques and tissue handling, making large, curated data sets scarce.[20] While deep learning excels at identifying patterns in high-resolution images, they are prone to errors, especially when presented with *systematic, nonstochastic* variations in staining quality and sample preparation protocols within training data. Current methods require human experts to verify automated cancer grading, highlighting the need for deep learning to complement rather than replace expert judgment in oncology.[21,22] Utilizing biochemically quantitative technologies that are less prone to sample preparation and staining variations is a promising route to achieving high diagnostic accuracy through AI. It is crucial for selecting appropriate treatments and improving patient outcomes.[23,24]

Midinfrared spectroscopic imaging (MIRSI) represents a class of technologies that offer biochemically sensitive, label-free imaging data. This approach addresses the aforementioned challenges with staining quality and quantification.[25−32] Furthermore, MIRSI provides data that can be interpreted in biochemical terms.[32−36] Optical photothermal infrared (O-PTIR) imaging[37−41] is emerging as a promising MIRSI technology that overcomes the diffraction-limited spatial resolution[42] characteristic of previous methods such as Fourier transform infrared (FTIR) spectroscopic imaging[43] and facilitating image capture at a resolution of 0.5 μm. Figure 1 illustrates the comparison between images at 1660 cm^{-1} obtained using FTIR and O-PTIR at their highest resolutions

of ~5 μm × 5 μm and 0.5 μm × 0.5 μm, respectively. FTIR resolution is wavenumber dependent whereas OPTIR is not. O-PTIR has a higher resolution and can visualize finer image details. However, a significant challenge with OPTIR is that hyperspectral data acquisition is time-consuming. To address the problem of slow data collection, we proposed a reconstruction algorithm for sparse data.[44] For instance, collecting an image at one wavelength for a 1400 μm × 1400 μm sample would previously take almost 80 min. We collected high-resolution images at one wavelength along with 27 low-resolution images at different wavelengths. Using curvelet transform and l_1 minimization, 27 low-resolution images were reconstructed while preserving spectral resolution. This research significantly enhances data collection speed, improving it 10-fold with minimal information loss. To validate this approach, we applied machine learning techniques to classify and segment ovarian cancer tissue, achieving a success rate of 95%. This approach makes hyperspectral photothermal (HP) MIRSI practical. Here, we build upon this work and expand the analysis of photothermal imaging data to address cervical tissue segmentation and the histopathological examination of multiple types of cervical cancer, including adenocarcinoma and squamous cell carcinoma. We will investigate the trade-off between image resolution and data acquisition time with hyperspectral MIRSI. We will combine data reconstruction with machine learning methods to facilitate tissue subtype classification across a wide range of cervical cancer samples. The use of photothermal MIRSI overcomes previous challenges associated with subcellular resolution. Our enhanced HP-MIRSI data collection approach addresses speed challenges and significantly accelerates the technology.

2. MATERIALS AND METHODS

Images were collected from a tissue microarray (TMA) of cervical biopsies from 100 patients, consisting of normal, adenocarcinoma, adenosquamous carcinoma, and squamous cell carcinoma samples (Biomax, CR1001b). The TMA was paraffin-embedded mounted on a 1 mm thickness CaF$_2$ substrate. The patient cohort consisted of women aged 23 to 76, with tumor stages ranging from I to IV. Paraffin-embedded samples were sectioned at 5 μm and deparaffinized prior to imaging. The deparaffinization was done following the protocol along the lines described in Baker et al.[33] before undergoing O-PTIR imaging. The paraffin-embedded samples were deparaffinized by washing the sample in 100% xylene twice for 5 min each and then with 100% ethanol thrice. Images were acquired from two adjacent sections of the TMA, one of which was labeled with hematoxylin and eosin (H&E) for annotation by a pathologist. The other immediate adjacent section was used for O-PTIR imaging after deparaffinization.

2.1. Data Acquisition

The adjacent H&E stained TMA was imaged with a Nikon inverted optical microscope with a 10×, 0.4 NA objective in the brightfield mode and has diffraction-limited spatial resolution in the visible range (0.4 μm to 0.7 μm). OPTIR data were collected using a Photothermal mIRage microscope with a silicon photodiode, a pixel size of 0.5 μm × 0.5 μm, and a 0.65 numerical aperture. A quantum cascade laser (QCL) source sweeps through the range of 902 cm^{-1} to 1898 cm^{-1}. We are using a 532 nm probe beam, and mIRage settings for data collection were 50% IR beam power with ≈100 kHz pulse rate, 5% duty cycle, and 500 ns pulse width. Detector gain was set at 10× and scan rate for each image was 0.4 Hz. We collected data with 0.5 μm × 0.5 μm spatial resolution per pixel at seven wavelengths: 1660, 1554, 1440, 1340, 1240, 1220, and 1104 cm^{-1}. Twenty-seven lower-resolution images were collected at a 0.5 μm × 5 μm per pixel at 974, 984, 1036, 1070, 1102, 1136, 1178, 1238, 1280, 1300, 1325, 1358, 1396, 1420, 1456, 1482, 1500, 1536, 1556, 1596, 1610, 1662,

1668, 1682, 1718, 1746, and 1786 cm^{-1}. Spectral bands are selected based on their biochemical importance.[33−35] Note that infrared spectra from biological samples often have broad peaks, and adjacent wavenumbers are frequently correlated. As a result, there is redundancy in the acquired data, which enhances the robustness of our results.

The average size for each biopsy was approximately 1400 × 1400 μm (Figure 1). Acquisition times were ≈80 min per band at high spatial resolution and ≈8 min per band at the lower spatial resolution. Capturing 7 high-resolution spectral wavenumbers took 9.3 h, whereas obtaining the 27 low-resolution plus 1 high-resolution image required 4.9 h. Subsequently, 27 high-resolution band images were reconstructed using our previously proposed algorithm[44] by combining low-resolution data with the high-resolution reference band at 1660 cm^{-1}. To minimize misalignment, all images were collected in one session. During data collection, we collected background and optimized the system every 6 h. Each core date was collected individually, and we focused the beam before each data collection to minimize any errors due to sample tilt. As a result of a stage shift during acquisition, portions of two cores were missing in some wavelengths. These cores were not included in the final analysis; therefore, all reported results pertain to 98 cores.

Two data cubes, with 27 and 7 bands, respectively, were produced for both the high-resolution and reconstructed images. A pathologist (Y.Z.) specializing in cervical cancer reviewed the corresponding adjacent section stained with H&E and annotated cell types from different disease stages. To develop the random forest (RF) and convolutional neural network (CNN) classifiers, one group of 44 cores was used for training, and another set of 54 different cores was used for testing. Both sets included multiple cancer grades. The structures of the RF and CNN classifiers are derived from our published work.[45−47] The last TMA row, which contained normal tissue, was used exclusively for testing, while for all other rows, the first five cores were used for training and the remaining cores for testing. This protocol ensures the independence of training and testing data sets, which is a limitation in previously published work.[45] Table 1 presents the number of pixels for each class in both training and testing.

Table 1. Number of O-PTIR Pixels in Training and Testing Datasets by Class[a]

class	training	testing
epithelium	7,790,150	10,104,774
stroma	12,571,675	11,509,787
total	20,361,825	21,614,561

[a]To create training and testing cohorts, the TMA is divided in half, with the left half used for training and the right half for testing. An equal number of pixels from each class is selected to avoid class-bias in training. Specifically, a subset of 10,000 O-PTIR pixels per class are utilized for training in the random forest (RF) classifier, and 400,000 pixels per class are employed for convolutional neural networks (CNNs).

2.2. Annotation

A pathologist annotated histological data based on images from an H&E stained adjacent section. The annotations included multiple tissue-type classes, such as stroma or epithelium. Even though the samples contained various tissue types, such as lymphocytes, blood cells, and necrosis, we limited our analysis to the two most abundant subtypes, namely epithelium and stroma, which appeared in nearly all the samples. Other tissue classes, being less abundant and having fewer annotation points, pose a challenge for identification using machine learning methods due to the limited amount of data. Moreover, to ensure robust training, the machine learning algorithms required us to label only those pixels of which we were absolutely certain. These annotations were then transferred to O-PTIR by manually aligning the chemically stained image with the correspond-

Table 2. Mean Accuracy of Models by Data Type Across Five Classification Experiments, Trained with 10,000 (RF) and 400,000 (CNN) Randomly Selected Samples Per Class[a]

class	RF7	RF27	CNN7	CNN27
epithelium	71.63 ± 1.29	81.42 ± 1.52	93.6 ± 2.3	97.88 ± 0.73
stroma	70.05 ± 1.21	72.24 ± 1.97	86.5 ± 2.2	92.62 ± 1.20
total	70.95 ± 0.72	76.53 ± 0.82	91 ± 0.9	94.98 ± 0.28

[a]The analysis compares classification results from 7 high-resolution bands with those from 27 reconstructed HP-MIRSI bands. The significantly higher accuracy of the CNN classifier is likely due to enhanced spatial resolution, which increases within-class spatial-spectral diversity. Moreover, a comparison between CNN27 and CNN7 demonstrates that our 27-band reconstruction approach, containing more spectroscopic information, achieves superior performance.

ing IR data. To create training and testing data sets, the left half of the TMA was used for training, while the right half was used for testing. This approach allowed the classifiers to be exposed to a variety of tissue types while maintaining independent training and testing sets.
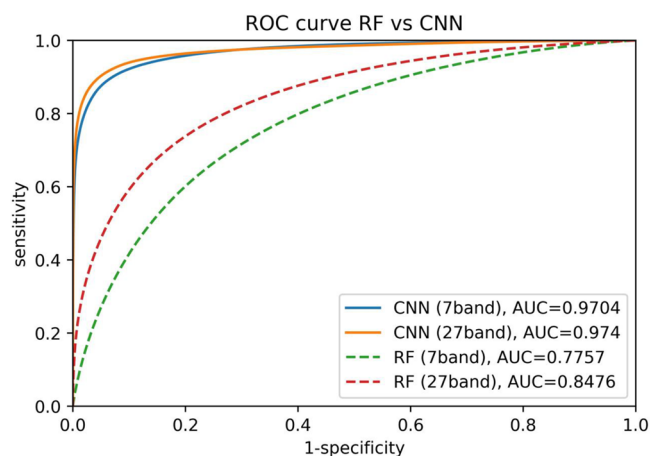
3. RESULTS

The overall accuracy (OA) and receiver operating characteristic (ROC) curves were used as evaluation metrics to evaluate the impact of improved spatial resolution in O-PTIR on cell type classification. The ROC curves delineate the correlation between specificity and sensitivity to ascertain acceptable false positive and true positive indicators.

The study evaluated the accuracy of two classifiers, RFs and CNNs, using data from both computationally reconstructed 27 high-resolution bands and 7 experimentally measured high-resolution bands. The detailed accuracy results, summarized in Table 2, revealed that the CNN classifier, which incorporates both spectral and spatial features from the O-PTIR data, consistently outperformed the RF classifier in overall and classwise accuracy, demonstrating a significant improvement of approximately 20% in overall accuracy. This increase is attributed to the CNN's ability to utilize a broader range of information, especially the high spatial resolution of photo-thermal MIRSI, compared to the RF's reliance on a limited set of spectral features. This is in line with our previous work[47] which only used 5 wavelengths and resulted in marginally lower accuracy. The enhanced performance with 27 bands, compared to 7, indicates that the reconstruction method not only shortens data collection time but also improves prediction accuracy by offering an expanded spectral data set. These findings highlight the critical role of combining spatial and spectral information in boosting classification accuracy.

Further analysis of classifier performance through a second measure, namely the area under the curve (AUC) in an ROC plot, presented in Figure 2, supports these conclusions. The 27-band CNN models exhibit superior performance over the 7-band configurations across both classes, reinforcing the value of integrating more comprehensive spectral features alongside spatial information for improved tissue classification accuracy.

Subsequently, we used our trained CNN models to segment all cores into tissue subtypes, including epithelium and stroma. The comparison of H&E images with the corresponding CNN predictions for 7 and 27 band data is illustrated in Figure 3. The 27 band classifier aligns more closely with the H&E images, suggesting that the reconstruction process effectively preserves information. This qualitative comparison provides a visual illustration and aligns well with the quantitative measures presented in Figure 2 and Table 2. Our optimized data collection and reconstruction approach not only optimizes data collection time but also improves accuracy in tissue subtype classification.


Figure 2. ROC curves and associated AUC values for each classification model. The CNN models (solid lines) yield superior results compared to the RF models (dashed lines) for both the 7-band and 27-band data sets. The enhanced performance of CNN models over RF is attributed to their utilization of both spatial and spectral information. Furthermore, CNN outcomes for the 27-band data set exhibit an improvement over the 7-band data set, owing to the increased spectral information.

We evaluated our 27-band CNN model on various subtypes of cervical cancer to further assess the segmentation efficacy of our method. The data set included 40 cores of squamous cell carcinoma and 26 cores of adenocarcinoma, and the remaining cores comprised other types, including adenosquamous carcinoma, endometrioid adenocarcinoma, mucinous adeno-carcinoma, and adjacent normal cervix tissues. For each cancer subtype, we loaded the pre trained model and tested it for three iterations to make sure results were robust and repeatable. The average accuracy and their standard deviation over three iterations are reported in Table 3. Additionally, we plotted the ROC curves for each cancer subtype, as presented in Figure 4. The AUC, an independent measure of classification accuracy, exceeds 0.95 for all subtypes. These results demonstrate good overall classification performance across all cervical cancer subclasses, although segmenting the stroma in squamous cell carcinoma presented the most significant challenge.

4. DISCUSSION

Our study demonstrates the utility of hyperspectral photo-thermal (HP) MIRSI, a technology that combines advanced computational techniques with quantitative, biochemically sensitive label-free contrast and subcellular resolution. This combination of advantages enables us to capture high-resolution images that are critical in distinguishing between different tissue types and identifying cancerous changes at the
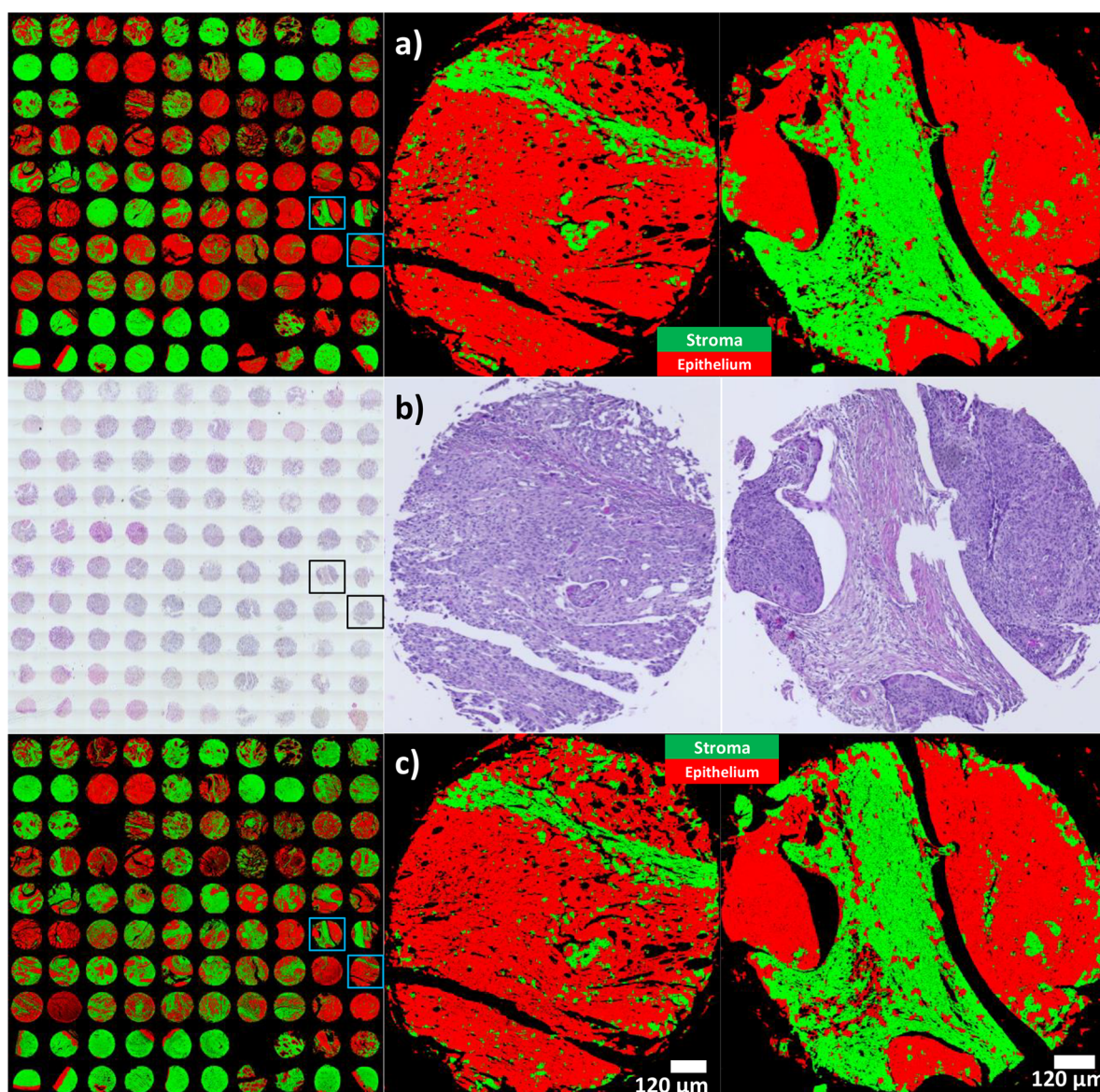
Figure 3. Comparison of classification results: (a) from the 7-band CNN, (b) from the H&E stained adjacent sections used to annotate ground truth, and (c) from the 27-band CNN. The 27-band CNN model exhibits a marginal yet noticeable improvement over the 7-band CNN results due to the increased number of bands. This supports and is consistent with the quantitative measures presented.

Table 3. Class Accuracies for Different Cervical Cancer Subtypes[a]

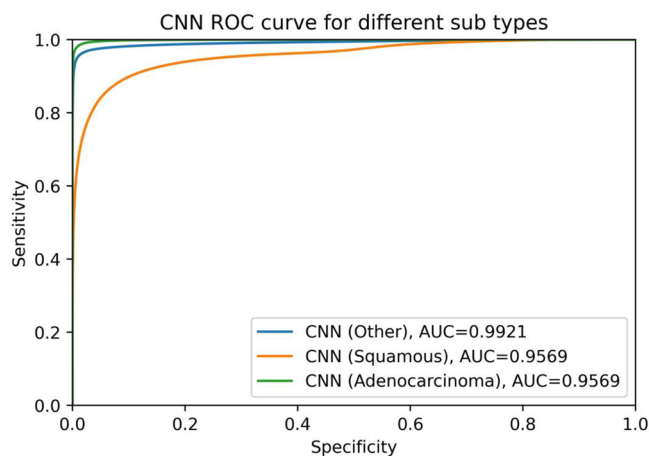| subtype	adenocarcinoma	squamous cell	other
epithelium pixels	759,291	5,991,556	1,987,103
epithelium accuracy	98.42 ± 0.85	95.30 ± 0.61	97.19 ± 1.52
stroma pixels	3,440,185	3,820,799	5,486,673
stroma accuracy	98.13 ± 0.79	80.46 ± 1.99	96.54 ± 0.73
total	98.15 ± 0.006	89.53 ± 0.011	96.72 ± 0.003

[a]The data included 40 cores with squamous cell carcinoma, 26 cores with adenocarcinoma, and other tissue that includes adenosquamous carcinoma, endometrioid adenocarcinoma, mucinous adenocarcinoma, and adjacent normal cervical tissues. The mean and standard deviation are reported below after testing the classifier for three iterations subtype.

cellular level. Our approach requires minimal tissue processing and does not use qualitative stains, making it a more efficient and practical method. Additionally, our optimized data acquisition and reconstruction approach reduces data collection time, making hyperspectral MIRSI data acquisition more feasible. We also utilize machine learning algorithms such as RF and CNN classifiers to improve the accuracy and efficiency of cervical tissue subtyping.

A key finding of our research is that HP-MIRSI can reliably segment multiple types of cervical cancer tissue into subtypes. We demonstrate >95% classification accuracy on a statically robust data set consisting of 98 cervical cancer patients and >40 million data points. Tissue subtype segmentation is a critical step in label-free diagnostics,[44,47] and our work lays the foundation for accurate, label-free cervical cancer diagnosis. This work is the first demonstration of applying high-resolution MIRSI to the challenging problem of cervical cancer tissue analysis. It promises a robust and quantitative alternative to current qualitative approaches.

Results from Tables 2 and 3 and the corresponding ROC curves show that CNNs have significant advantages over RF classifiers with segmenting photothermal MIRSI data. This can

Figure 4. ROC curves and associated AUC values for different cervical cancer subtypes. The data set comprised 40 cores with squamous cell carcinoma, 26 cores with adenocarcinoma, and other tissues, including adenosquamous carcinoma, endometrioid adenocarcinoma, mucinous adenocarcinoma, and adjacent normal cervical tissues. The AUC values for all cancer subtypes exceed 0.95, indicating high tissue segmentation performance across various cancer tissues.

be intuitively understood as a consequence of the higher resolution (0.5 μm) and the corresponding increased spatial details available in photothermal images. CNNs are capable of leveraging spatial details to improve classification, whereas RFs that rely on spectral information alone cannot achieve the same gains.

Our optimized data collection and reconstruction approach[44] for analyzing cervical cancer tissues shows remarkable efficacy, as evidenced by the superior performance of CNN models in classifying these tissues (see Table 2). This approach, which combines low- and high-resolution imaging from 27 bands with data reconstruction, outperforms the use of 7 high-resolution bands alone. Additionally, the process of obtaining data from the 27 bands required only 4.9 h, compared to the 9.3 h needed to obtain the 7 high-resolution band data, further demonstrating the efficiency of our method. Our work significantly reduces data collection time in HP-MIRSI without compromising spectral data quality and demonstrates excellent *automated* segmentation of *clinical* cervical cancer tissue. This advancement not only improves the feasibility of implementing HP-MIRSI in clinical environments by overcoming numerous barriers to its adoption but also paves the way for real-time cancer diagnosis and treatment planning.

We present the results of tissue type segmentation for multiple subtypes of cervical cancer, including squamous cell carcinoma and adenocarcinoma, in Table 3 and Figure 4. Utilizing large data sets with 98 cervical cancer patients allows us to analyze cervical cancer subtypes in a robust manner, with 40 patients having squamous cell carcinoma, 26 patients with adenocarcinoma, and the rest with adenosquamous carcinoma, endometrioid adenocarcinoma, mucinous adenocarcinoma, and adjacent normal cervix tissues. The segmentation and analysis, conducted with over 40 million data points, yield statistically reliable results. Moreover, the segmentation results exhibit a close alignment with H&E-stained data presented in Figure 3. The accuracy of our results is supported by both

quantitative and qualitative assessments of tissue segmentation, elucidating the reliability of our findings.

5. CONCLUSION

Our research introduces a novel method for the rapid and accurate analysis of cervical cancer tissue, leveraging the strengths of HP-MIRSI and advanced machine learning algorithms. This study demonstrates the potential of our approach in rapid, quantitative, label-free, digital histopathology. Our work is an important step in the clinical translation of this technology and its wider deployment. This technology has the potential to provide fast and reliable tissue diagnostics with minimal sample preparation. The implications of our work extend beyond cervical cancer, offering a promising avenue for the application of this technology in the early detection and classification of multiple cancer types. Future research will focus on refining the technology and exploring its integration into clinical practice, with the ultimate goal of improving patient outcomes through early and accurate diagnosis.

■ AUTHOR INFORMATION

Corresponding Author

Rohith Reddy − *Department of Electrical and Computer Engineering, University of Houston, Houston, Texas 77030, United States*; Present Address: 4226 Martin Luther King Blvd., N308 Engineering Building 1, Houston, TX 77584; ◉ orcid.org/0000-0002-4403-5614; Email: rkreddy@uh.edu

Authors

Reza Reihanisaransari − *Department of Electrical and Computer Engineering, University of Houston, Houston, Texas 77030, United States*

Chalapathi Charan Gajjela − *Department of Electrical and Computer Engineering, University of Houston, Houston, Texas 77030, United States*

Xinyu Wu − *Department of Electrical and Computer Engineering, University of Houston, Houston, Texas 77030, United States*

Ragib Ishrak − *Department of Electrical and Computer Engineering, University of Houston, Houston, Texas 77030, United States*

Yanping Zhong − *The University of Texas MD Anderson Cancer Center, Houston, Texas 77030, United States*; Present Address: Department of Pathology, The First Hospital of Jilin University, Changchun 130021, Jilin, China

David Mayerich − *Department of Electrical and Computer Engineering, University of Houston, Houston, Texas 77030, United States*; ◉ orcid.org/0000-0002-3949-6133

Sebastian Berisha − *Milwaukee School of Engineering, Milwaukee, Wisconsin 53202, United States*

Complete contact information is available at:
https://pubs.acs.org/10.1021/cbmi.4c00031

Author Contributions

R.R.S.: Data curation, formal analysis, investigation, methodology, writing - original draft preparation. C.C.G.: Data curation, visualization, investigation. X.W.: Methodology, investigation, visualization. R.I.: Resources, software. Y.G.: Data curation, D.M.: Writing - reviewing and editing. S.B.: Investigation, methodology, software, validation. R.R.: Con-

ceptualization, funding acquisition, project administration, resources, supervision, writing - reviewing and editing.

Notes

The authors declare no competing financial interest.

■ REFERENCES

(1) Sung, H.; Ferlay, J.; Siegel, R. L.; Laversanne, M.; Soerjomataram, I.; Jemal, A.; Bray, F. Global Cancer Statistics 2020: GLOBOCAN Estimates of Incidence and Mortality Worldwide for 36 Cancers in 185 Countries. *CA: a cancer journal for clinicians* **2021**, *71*, 209−249.

(2) Stelzle, D.; Tanaka, L. F.; Lee, K. K.; Ibrahim Khalil, A.; Baussano, I.; Shah, A. S. V.; McAllister, D. A.; Gottlieb, S. L.; Klug, S. J.; Winkler, A. S.; Bray, F.; Baggaley, R.; Clifford, G. M.; Broutet, N.; Dalal, S. Estimates of the global burden of cervical cancer associated with HIV. *Lancet Global Health* **2021**, *9*, e161−e169.

(3) Arbyn, M.; Weiderpass, E.; Bruni, L.; de Sanjosé, S.; Saraiya, M.; Ferlay, J.; Bray, F. Estimates of incidence and mortality of cervical cancer in 2018: a worldwide analysis. *Lancet Global Health* **2020**, *8*, e191−e203.

(4) Momenimovahed, Z.; Mazidimoradi, A.; Maroofi, P.; Allahqoli, L.; Salehiniya, H.; Alkatout, I. Global, regional and national burden, incidence, and mortality of cervical cancer. *Cancer Reports (Hoboken, N.J.)* **2023**, *6*, No. e1756.

(5) Tsu, V. D.; LaMontagne, D. S.; Atuhebwe, P.; Bloem, P. N.; Ndiaye, C. National implementation of HPV vaccination programs in low-resource countries: Lessons, challenges, and future prospects. *Preventive Medicine* **2021**, *144*, 106335.

(6) Gates, A.; Pillay, J.; Reynolds, D.; Stirling, R.; Traversy, G.; Korownyk, C.; Moore, A.; Thériault, G.; Thombs, B. D.; Little, J.; Popadiuk, C.; van Niekerk, D.; Keto-Lambert, D.; Vandermeer, B.; Hartling, L. Screening for the prevention and early detection of cervical cancer: protocol for systematic reviews to inform Canadian recommendations. *Systematic Reviews* **2021**, *10*, 2.

(7) Peirson, L.; Fitzpatrick-Lewis, D.; Ciliska, D.; Warren, R. Screening for cervical cancer: a systematic review and meta-analysis. *Systematic Reviews* **2013**, *2*, 35.

(8) Moarcăs, M.; Georgescu, I.; Brătilă, E.; Badea, M.; Cîrstoiu, E. Clinical significance of HPV-DNA testing for precancerous cervical lesionS. *Journal of Medicine and Life* **2014**, *7*, 37−39.

(9) Terasawa, T.; Hosono, S.; Sasaki, S.; Hoshi, K.; Hamashima, Y.; Katayama, T.; Hamashima, C. Comparative accuracy of cervical cancer screening strategies in healthy asymptomatic women: a systematic review and network meta-analysis. *Sci. Rep.* **2022**, *12*, 94.

(10) Cafforio, P.; Palmirotta, R.; Lovero, D.; Cicinelli, E.; Cormio, G.; Silvestris, E.; Porta, C.; D'Oronzo, S. Liquid Biopsy in Cervical Cancer: Hopes and Pitfalls. *Cancers* **2021**, *13*, 3968.

(11) Herbst, J.; Pantel, K.; Effenberger, K.; Wikman, H. Clinical applications and utility of cell-free DNA-based liquid biopsy analyses in cervical cancer and its precursor lesions. *Br. J. Cancer* **2022**, *127*, 1403−1410. Publisher: Nature Publishing Group.

(12) Wang, J.; Zheng, C.-X.; Ma, C.-L.; Zheng, X.-X.; Lv, X.-Y.; Lv, G.-D.; Tang, J.; Wu, G.-H. Raman spectroscopic study of cervical precancerous lesions and cervical cancer. *Lasers in Medical Science* **2021**, *36*, 1855−1864.

(13) Wang, X.; Wang, Y.; Zhang, Z.; Huang, M.; Fei, Y.; Ma, J.; Mi, L. Discriminating different grades of cervical intraepithelial neoplasia based on label-free phasor fluorescence lifetime imaging microscopy. *Biomedical Optics Express* **2020**, *11*, 1977−1990.

(14) Ji, M.; Zhong, J.; Xue, R.; Su, W.; Kong, Y.; Fei, Y.; Ma, J.; Wang, Y.; Mi, L. Early Detection of Cervical Cancer by Fluorescence Lifetime Imaging Microscopy Combined with Unsupervised Machine Learning. *International Journal of Molecular Sciences* **2022**, *23*, 11476.

(15) Prabitha, V. G.; Suchetha, S.; Jayanthi, J. L.; Baiju, K. V.; Rema, P.; Anuraj, K.; Mathews, A.; Sebastian, P.; Subhash, N. Detection of cervical lesions by multivariate analysis of diffuse reflectance spectra: a clinical study. *Lasers in Medical Science* **2016**, *31*, 67−75.

(16) Mehmood, M.; Rizwan, M.; Abbas, S. Machine Learning Assisted Cervical Cancer Detection. *Frontiers in Public Health* **2021**, *9*, No. 788376.

(17) Bengtsson, E.; Malm, P. Screening for Cervical Cancer Using Automated Analysis of PAP-Smears. *Computational and Mathematical Methods in Medicine* **2014**, *2014*, No. e842037.

(18) Chankong, T.; Theera-Umpon, N.; Auephanwiriyakul, S. Automatic cervical cell segmentation and classification in Pap smears. *Computer Methods and Programs in Biomedicine* **2014**, *113*, 539−556.

(19) Hou, X.; Shen, G.; Zhou, L.; Li, Y.; Wang, T.; Ma, X. Artificial Intelligence in Cervical Cancer Screening and Diagnosis. *Frontiers in Oncology* **2022**, *12*, 851367.

(20) Hussain, E.; Mahanta, L. B.; Das, C. R.; Choudhury, M.; Chowdhury, M. A shape context fully convolutional neural network for segmentation and classification of cervical nuclei in Pap smear images. *Artificial Intelligence in Medicine* **2020**, *107*, 101897.

(21) Tran, K. A.; Kondrashova, O.; Bradley, A.; Williams, E. D.; Pearson, J. V.; Waddell, N. Deep learning in cancer diagnosis, prognosis and treatment selection. *Genome Medicine* **2021**, *13*, 152.

(22) Koh, D. M.; et al. Artificial intelligence and machine learning in cancer imaging. *Communications Medicine* **2022**, *2*, No. 133.

(23) Cao, W.; Rocha, H.; Mohan, R.; Lim, G.; Goudarzi, H. M.; Ferreira, B. C.; Dias, J. M. Reflections on beam configuration optimization for intensity-modulated proton therapy. *Physics in Medicine & Biology* **2022**, *67*, 13TR01.

(24) Goudarzi, H. M.; Lim, G.; Grosshans, D.; Mohan, R.; Cao, W. Incorporating variable RBE in IMPT optimization for ependymoma. *Journal of Applied Clinical Medical Physics* **2024**, *25*, No. e14207.

(25) Mankar, R.; Gajjela, C. C.; Bueso-Ramos, C. E.; Yin, C. C.; Mayerich, D.; Reddy, R. K. Polarization Sensitive Photothermal Mid-Infrared Spectroscopic Imaging of Human Bone Marrow Tissue. *Appl. Spectrosc.* **2022**, *76*, 508−518.

(26) Reddy, R. K.; Bhargava, R. Accurate histopathology from low signal-to-noise ratio spectroscopic imaging data. *Analyst* **2010**, *135*, 2818−2825.

(27) Walsh, M. J.; Reddy, R. K.; Bhargava, R. Label-free biomedical imaging with mid-IR spectroscopy. *IEEE J. Sel. Top. Quantum Electron.* **2012**, *18*, 1502−1513.

(28) Kole, M. R.; Reddy, R. K.; Schulmerich, M. V.; Gelber, M. K.; Bhargava, R. Discrete frequency infrared microspectroscopy and imaging with a tunable quantum cascade laser. *Analytical chemistry* **2012**, *84*, 10366−10372.

(29) Yeh, K.; Lee, D.; Bhargava, R. Multicolor discrete frequency infrared spectroscopic imaging. *Analytical chemistry* **2019**, *91*, 2177−2185.

(30) Yeh, K.; Sharma, I.; Falahkheirkhah, K.; Confer, M. P.; Orr, A. C.; Liu, Y.-T.; Phal, Y.; Ho, R.-J.; Mehta, M.; Bhargava, A.; et al. others Infrared spectroscopic laser scanning confocal microscopy for whole-slide chemical imaging. *Nat. Commun.* **2023**, *14*, 5215.

(31) Yeh, K.; Kenkel, S.; Liu, J.-N.; Bhargava, R. Fast infrared chemical imaging with a quantum cascade laser. *Analytical chemistry* **2015**, *87*, 485−493.

(32) Pahlow, S.; Weber, K.; Popp, J.; Wood, B. R.; Kochan, K.; Rüther, A.; Perez-Guaita, D.; Heraud, P.; Stone, N.; Dudgeon, A.; et al. others Application of vibrational spectroscopy and imaging to point-of-care medicine: A review. *Applied spectroscopy* **2018**, *72*, 52−84.

(33) Baker, M. J.; Trevisan, J.; Bassan, P.; Bhargava, R.; Butler, H. J.; Dorling, K. M.; Fielden, P. R.; Fogarty, S. W.; Fullwood, N. J.; Heys,

K. A.; et al. others Using Fourier transform IR spectroscopy to analyze biological materials. *Nature protocols* **2014**, *9*, 1771.

(34) Fernandez, D. C.; Bhargava, R.; Hewitt, S. M.; Levin, I. W. Infrared spectroscopic imaging for histopathologic recognition. *Nature biotechnology* **2005**, *23*, 469−474.

(35) Pounder, F. N.; Reddy, R. K.; Bhargava, R. Development of a practical spatial-spectral analysis protocol for breast histopathology using Fourier transform infrared spectroscopic imaging. *Faraday Discuss.* **2016**, *187*, 43−68.

(36) Llorá, X.; Reddy, R.; Matesic, B.; Bhargava, R. Towards better than human capability in diagnosing prostate cancer using infrared spectroscopic imaging. *Proceedings of the 9th annual conference on Genetic and evolutionary computation*; 2007; pp 2098−2105.

(37) Zhang, D.; Li, C.; Zhang, C.; Slipchenko, M. N.; Eakins, G.; Cheng, J.-X. Depth-resolved mid-infrared photothermal imaging of living cells and organisms with submicrometer spatial resolution. *Science advances* **2016**, *2*, No. e1600521.

(38) Bialkowski, S. *Photothermal spectroscopy methods for chemical analysis*; John Wiley & Sons, 1996; Vol. *134*.

(39) Bai, Y.; Zhang, D.; Lan, L.; Huang, Y.; Maize, K.; Shakouri, A.; Cheng, J.-X. Ultrafast chemical imaging by widefield photothermal sensing of infrared absorption. *Science advances* **2019**, *5*, No. eaav7127.

(40) Xia, Q.; Yin, J.; Guo, Z.; Cheng, J.-X. Mid-infrared photothermal microscopy: principle, instrumentation, and applications. *J. Phys. Chem. B* **2022**, *126*, 8597−8613.

(41) Bai, Y.; Yin, J.; Cheng, J.-X. Bond-selective imaging by optically sensing the mid-infrared photothermal effect. *Science advances* **2021**, *7*, No. eabg1559.

(42) Reddy, R. K.; Walsh, M. J.; Schulmerich, M. V.; Carney, P. S.; Bhargava, R. High-definition infrared spectroscopic imaging. *Applied spectroscopy* **2013**, *67*, 93−105.

(43) Lewis, E. N.; Treado, P. J.; Reeder, R. C.; Story, G. M.; Dowrey, A. E.; Marcott, C.; Levin, I. W. Fourier transform spectroscopic imaging using an infrared focal-plane array detector. *Analytical chemistry* **1995**, *67*, 3377−3381.

(44) Reihanisaransari, R.; Gajjela, C. C.; Wu, X.; Ishrak, R.; Corvigno, S.; Zhong, Y.; Liu, J.; Sood, A. K.; Mayerich, D.; Berisha, S.; Reddy, R. Rapid hyperspectral photothermal mid-infrared spectroscopic imaging from sparse data for gynecologic cancer tissue subtyping. 2024; http://arxiv.org/abs/2402.17960, arXiv:2402.17960 [cs, q-bio].

(45) Lotfollahi, M.; Berisha, S.; Daeinejad, D.; Mayerich, D. Digital staining of high-definition Fourier transform infrared (FT-IR) images using deep learning. *Applied spectroscopy* **2019**, *73*, 556−564.

(46) Lotfollahi, M.; Tran, N.; Gajjela, C.; Berisha, S.; Han, Z.; Mayerich, D.; Reddy, R. Adaptive Compressive Sampling for Mid-Infrared Spectroscopic Imaging. *2022 IEEE International Conference on Image Processing (ICIP)*; 2022; pp 2336−2340.

(47) Gajjela, C. C.; Brun, M.; Mankar, R.; Corvigno, S.; Kennedy, N.; Zhong, Y.; Liu, J.; Sood, A. K.; Mayerich, D.; Berisha, S.; et al. others Leveraging mid-infrared spectroscopic imaging and deep learning for tissue subtype classification in ovarian cancer. *Analyst* **2023**, *148*, 2699−2708.